Nanoplasmonic Probes of Catalytic Reactions

Elin M. Larsson, *et al.*

Science **326**, 1091 (2009);
DOI: 10.1126/science.1176593

the case. Moreover, robust Re-Os age constraints on peridotitic diamonds from the harzburgitic layer suggest that the central Slave's lithospheric mantle down to 150 km was formed and stabilized by 3.5 Ga (*22*). Therefore, the central Slave seismic discontinuity is likely caused by metasomatized mantle from a Paleoarchean subduction zone.

The presence of a Paleoarchean cratonic lithosphere in the Slave does not conflict with the occurrence of craton-wide arc volcanism and plutonism during later Neoarchean time (*21*); rather, it suggests that the blocks that aggregated in the final stage of cratonic assembly may themselves have been fragments of older, thick proto-cratonic entities. This is consistent with the limited lateral extent of the discontinuity, which may mark the outline of a broken block (fig. S4), and is supported by the unique geochemical signature and high concentration of diamondiferous kimberlites found in the same region (*2*).

If subduction has been active since the Paleoarchean, similar or related structures with limited lateral extent should be expected in other parts of the craton and in other cratons worldwide. Indeed, anisotropic seismic discontinuities have been detected below the southwest edge of the Slave craton (*4*) and the adjacent Wopmay orogen (*23*). These have been inferred to mark Proterozoic collision-subduction events associated with the final assembly and stabilization of a large part of the Laurentian continent (*24*). Away from cratonic edges, similar seismic discontinuities have been detected in the Kaapvaal craton of South Africa (*25*). Moreover, a global compilation of long-aperture seismic refraction data indicates the existence of a widespread (albeit not ubiquitous) negative discontinuity in the 90- to 120-km depth range beneath several Archean cratons (*26*). The character of the discontinuities (i.e., their spatial extent, depth, dip, and physical properties) depends on the details of each subduction event, including the amount of metasomatism, the subduction geometry, and history of much younger events of accretion and magmatism. Given the limited detailed geophysical sampling of cratons and the nonuniform nature of these subduction-related discontinuities, it is thus not surprising that not many of them have been observed to date.

References and Notes

1. S. A. Bowring, I. S. Williams, W. Compston, *Geology* **17**, 971 (1989).
2. W. L. Griffin *et al.*, *J. Petrol.* **40**, 705 (1999).
3. H. S. Grütter, D. B. Apter, J. Kong, in *Proceedings of the 7th International Kimberlite Conference*, J. J. Gurney *et al.*, Eds. (Red Roof Design, Cape Town, 1999), vol. 1, pp. 307–313.
4. M. G. Bostock, *J. Geophys. Res.* **103**, 21183 (1998).
5. D. B. Snyder, *Tectonics* **27**, TC4006 (2008).
6. M. Moorkamp, A. G. Jones, D. W. Eaton, *Geophys. Res. Lett.* **34**, L16311 (2007).
7. H. H. Helmstaedt, J. D. Schulze, in *Kimberlites and Related Rocks, Their Composition, Occurrence, Origin, and Emplacement*, J. Ross, Ed. (Geological Society of Australia, Canberra, 1989), vol. 1, pp. 358–368.
8. T. H. Jordan, *Nature* **274**, 544 (1978).
9. Supporting material is available on *Science* Online.
10. A. G. Jones *et al.*, *Geology* **29**, 423 (2001).
11. C.-T. A. Lee, *J. Geophys. Res.* **108**, 2441 (2003).
12. A. G. Jones, R. L. Evans, D. W. Eaton, *Lithos* **109**, 131 (2009).
13. D. E. Boerner *et al.*, *Science* **283**, 668 (1999).
14. S. Aulbach, N. J. Pearson, S. Y. O'Reilly, B. J. Doyle, *J. Petrol.* **48**, 1843 (2007).
15. B. R. Hacker *et al.*, *J. Petrol.* **46**, 1661 (2005).
16. A. A. Guseinov, I. O. Gargatsev, R. U. Gabitova, *Izv. Phys. Solid Earth* **41**, 670 (2005).
17. M. Mareschal, W. S. Fyfe, J. Percival, T. Chan, *Nature* **357**, 674 (1992).
18. D. M. Kerrick, J. A. D. Connolly, *Nature* **411**, 293 (2001).
19. C.-T. A. Lee, in *Archean Geodynamics and Environments*, K. Benn, J.-C. Mareschal, K. C. Condie, Eds. (American Geophysical Union, Washington, DC, 2006), vol. 164, pp. 89–114.
20. L. S. Wagner, S. Beck, G. Zandt, M. N. Ducea, *Earth Planet. Sci. Lett.* **245**, 289 (2006).
21. W. J. Davis, A. G. Jones, W. Bleeker, H. Grütter, *Lithos* **71**, 575 (2003).
22. K. J. Westerlund *et al.*, *Contrib. Mineral. Petrol.* **152**, 275 (2006).
23. J.-P. Mercier *et al.*, *J. Geophys. Res.* **113**, B04308 (2008).
24. P. F. Hoffman, *Annu. Rev. Earth Planet. Sci.* **16**, 543 (1988).
25. D. B. Snyder, S. Rondenay, M. G. Bostock, G. D. Lockhart, *Lithos* **77**, 859 (2004).
26. H. Thybo, E. Perchuć, *Science* **275**, 1626 (1997).
27. W. Bleeker, L. Ketchum, V. Jackson, M. Villeneuve, *Can. J. Earth Sci.* **36**, 1083 (1999).

28. We thank S. Bowring for thoughtful and insightful comments on earlier drafts of this paper. We thank A. Jones for permission to use his figure in Fig. 2B. We thank S. Shirey, S. Aulbach, C. Till, L. Elkins-Tanton, and M. Moorkamp for helpful discussions, the POLARIS consortium for making data available, and members in the Northwest Territories Geoscience Office, BHP-Billiton Diamonds Inc., De Beers Canada Inc., and Tahera Diamond Corp. for logistical support of our field work in the Slave province. This work is funded by NSF grant EAR-0409509 (S.R.). C.-W.C. is partially supported by an MIT Praecis Presidential Fellowship. This is Natural Resources Canada Earth Sciences Sector (ESS) contribution 20090244.

Supporting Online Material

www.sciencemag.org/cgi/content/full/326/5956/1089/DC1
SOM Text
Figs. S1 to S4
Table S1
References

30 June 2009; accepted 17 September 2009
10.1126/science.1178477

Nanoplasmonic Probes of Catalytic Reactions

Elin M. Larsson,* Christoph Langhammer, Igor Zorić, Bengt Kasemo

Optical probes of heterogeneous catalytic reactions can be valuable tools for optimization and process control because they can operate under realistic conditions, but often probes lack sensitivity. We have developed a plasmonic sensing method for such reactions based on arrays of nanofabricated gold disks, covered by a thin (~10 nanometer) coating (catalyst support) on which the catalyst nanoparticles are deposited. The sensing particles monitor changes in surface coverage of reactants during catalytic reaction through peak shifts in the optical extinction spectrum. Sensitivities to below 10^{-3} monolayers are estimated. The capacity of the method is demonstrated for three catalytic reactions, CO and H_2 oxidation on Pt, and NO_x conversion to N_2 on Pt/BaO.

In heterogeneous catalysis, reactants in gas or liquid phase are converted to desired product molecules on the surface of a solid catalyst, which is usually composed of catalytically active nanoparticles (1 to 10 nm) dispersed on a porous, high-surface-area support material. In order to understand and improve these systems, it is important to be able to monitor the catalyst's state and to follow the reaction in real time. An important quantity is the surface coverage of reactants. However, experimental difficulties arise from the complexity of the catalyst and the atmospheric or higher pressures in which the reactions occur. Model systems (commonly single-crystal surfaces) and model reactions are frequently investigated at idealized ultrahigh vacuum (UHV) conditions, allowing use of powerful experimental probes (such as electrons, photons, or ions). A major challenge is to correlate results obtained by using the idealized and thoroughly scrutinized model catalysts in UHV with those of the less characterized real nanostructured catalysts at real reaction conditions (*1*–*3*).

We describe a method that, with a simple optical transmission (or reflection) measurement (Fig. 1A), can follow catalytic reactions in real time for both model and real supported catalysts. The principle is "nanoplasmonic" [localized surface plasmon resonance (LSPR)] sensing, currently intensely explored for biosensing, down toward single-molecule sensitivity (*4*). We show that LSPR can monitor changes in adsorbate coverages on "realistic" supported catalysts (Fig. 2) with a sensitivity corresponding to much less than 0.1 monolayer (ML).

For demonstrators, we used two types of Pt catalysts (Fig. 1, B to G) and three well-known catalytic reactions: oxidation of hydrogen ($H_2 + 1/2O_2 \rightarrow H_2O$), oxidation of carbon monoxide ($CO + 1/2O_2 \rightarrow CO_2$), and NO_x storage and

Chemical Physics Group, Department of Applied Physics, Chalmers University of Technology, SE-41296 Gothenburg, Sweden.

*To whom correspondence should be addressed. E-mail: elarsson@chalmers.se

reduction over Pt/BaO catalysts. The first reaction is a common model reaction (*5*) relevant for hydrogen fuel cells, whereas the latter two are of key importance in automotive emission cleaning (*1*, *6*).

An optical transmission measurement (Fig. 1A) is made through a quartz reactor in which a transparent sample is mounted (alternatively, measurements can be made in reflection). The sample consists of the LSPR sensing structure and the catalyst, deposited on a glass substrate by using nanofabrication techniques and evaporation (Fig. 1, B to G). The transmission of white light through the sample, via the reactor walls, was detected as a function of wavelength by use of an array spectrometer (*7*). In some cases, scanning the spectral region of interest with monochromatic light or measuring the extinction at a particular wavelength may be preferable. This technique is suitable for use in either harsh environments, a remote sensing setup, or both.

The LSPR sensing structures are, in the present work, nanoscale disks of gold or platinum. The light transmitted through the sample has an intensity minimum (maximum extinction) at the wavelength at which the LSPR excitation in the sensing particles is strongest (Fig. 1A, bottom). The excitation creates a strongly enhanced electromagnetic near field, which acts as a probe of the nanoparticle's surrounding (*8*). The wavelength of maximum extinction, λ_{max}, is very sensitive to changes of the dielectric properties near the sensing nanoparticles [within a few tens of nanometers; see discussion below and in (*7*)]. It is the shift of λ_{max}, measured with a resolution of 0.01 nm, that provides the sensing function (Fig. 1A, bottom) and allows sub-monolayer changes in surface coverage to be monitored.

For the Pt-catalyzed oxidation of hydrogen, we used a sample (Fig. 1, B to D) consisting of an array of nanofabricated (*9*) plasmonic gold disks ($\lambda_{max} \approx 570$ nm, 76 nm diameter, and 30 nm high) that were covered by a 10-nm-thick film of SiO_2, on which a nanogranular Pt catalyst was deposited by means of electron-beam evaporation. The amount of Pt is small enough so that individual Pt nanoparticles of sizes in the range of 5 to 20 nm are formed (see Fig. 1D) (*7*), which mimics the size range of real supported Pt catalysts. We call this sensing method "indirect sensing" (*10*) because in this case the LSPR sensing structure is not the catalyst, contrary to the case in a previous demonstration by Novo *et al*., of using gold nanocrystals as both catalysts and LSPR sensor to follow a liquid-phase charge-transfer reaction (*11*).

The experiment was performed by slowly varying the relative H_2 concentration, $\alpha^{H2} = [H_2]/([H_2] + [O_2])$, from hydrogen-rich to oxygen-rich and back again while continuously recording $\Delta\lambda_{max}$ (Fig. 2A) (*7*). The H_2 scan rate was slow enough so that steady state was established at each concentration, except possibly for very slow structural or chemical changes of the catalyst. The sample temperature was measured with a thermocouple in contact with the sample surface. The reactant ($H_2 + O_2$) concentration was kept constant at 4% in Ar carrier gas at atmospheric pressure by means of a gas flow of 16.7 ml/s (3.4 cm/s plug flow velocity). The sample temperature (T), without reaction, was 509 K.

We observed discontinuous steps up and down in $\Delta\lambda_{max}$ at a critical reactant mixture of $\alpha^{H2}_{cr} = 0.5$ (Fig. 2A, blue curves), depending on whether the H_2 fraction was increasing or decreasing. This step is completely absent in control measurements on an identical structure without Pt particles. The step in $\Delta\lambda_{max}$ coincides with a peak ($\Delta T_{max} = 16$ K) in the simultaneously measured sample temperature (Fig. 2A, red and brown curves), which is caused by the exothermicity of the reaction. $\Delta\lambda_{max}$ varies only slowly above and below α^{H2}_{cr}. All data measured with the sample structure in Fig. 1B were corrected for a small background signal, which was caused by the interaction of reactant gases with the SiO_2 surface (*7*, *12*). This correction slightly affects the slopes of $\Delta\lambda_{max}$ on both sides of α^{H2}_{cr} but does not affect the position or magnitude of the step in $\Delta\lambda_{max}$.

The $\Delta\lambda_{max}$ step is assigned to the well-known kinetic phase transition in the $H_2 + O_2$ reaction, occurring at a critical gas mixture, α^{H2}_{cr}, at which a sudden transition occurs from an oxygen-covered surface at low α^{H2} to a partially hydrogen-covered surface at high α^{H2} (*13*). This transition occurs where the overall exothermic reaction has a rate maximum, which is the reason for the peak in temperature.

Because the kinetic phase transition at $\alpha^{H2} = \alpha^{H2}_{cr}$ involves a transition from an essentially oxygen-saturated to a partially hydrogen-covered surface, this example shows that LSPR can (i) detect surface coverage changes at the sub-monolayer level on small supported Pt nanoparticles and (ii) follow the kinetics of a catalytic reaction. The slopes of the LSPR peak position versus α^{H2}, on both sides of the kinetic phase transition, are not primarily due to coverage changes but are the result of the reaction-induced temperature variation (*14*). This effect can, if needed, be subtracted by separate calibration measurements of $\Delta\lambda_{max}$ versus temperature with a non-reactive gas. The fact that the LSPR resonance position is also sensitive to temperature has, however, no influence on the measured $\Delta\lambda_{max}$ step at α^{H2}_{cr}. The temperature variation over the region of the step is minor and estimated to be less than 1 K. Raw data of the LSPR resonance position versus time (as α was changed), and the accompanying temperature change, is shown in fig. S3. According to these data, the $\Delta\lambda_{max}$ step at the kinetic phase transition point is not compromised by temperature (see also the next example), which essentially is constant over that narrow α regime.

Further proof that the temperature sensitivity of $\Delta\lambda_{max}$ does not affect the step in $\Delta\lambda_{max}$ at the kinetic phase transition was obtained from measurements with diluted reactant concentrations of $H_2 + O_2$, from 6 to 1% (fig. S5). Such dilution did not change the magnitude of the $\Delta\lambda_{max}$ step at all (as expected, if it is due to a coverage change from or to a saturated oxygen adlayer) but changed the maximum temperature rise from 4 K to 24 K because of the increasing chemical power generation at higher concentrations. The temperature sensitivity of the LSPR, which at first sight might seem as a complication, can be used for an independent LSPR-based temperature measurement, as discussed in (*7*).

In the above measurements, there was potentially a difference in the temperature measured by the thermocouple and the actual catalyst particle temperature because of very local temperature gradients. However, this does not change the general analysis or conclusions above because such a gradient if at all present would not change the analysis at the kinetic phase transition (which is the most important part).

Qualitatively similar results with larger Pt particles were also obtained for "direct sensing," in which Pt disks were simultaneously acting as the catalyst and the LSPR-sensing particles (*7*). Pt nanoparticles have previously been found to exhibit optical excitations similar to those of Au nanoparticles (*15*). In some cases, this type of sensing—which is somewhat similar to the results by Novo *et al.* (*11*)—may be preferred because, for example, the Pt disks can be converted to well-defined single crystals (*16*) and thus can represent model catalysts. However, here our focus and emphasis is on the indirect sensing, in which the sensing particles are not the catalyst, because this is a much more versatile and entirely new approach.

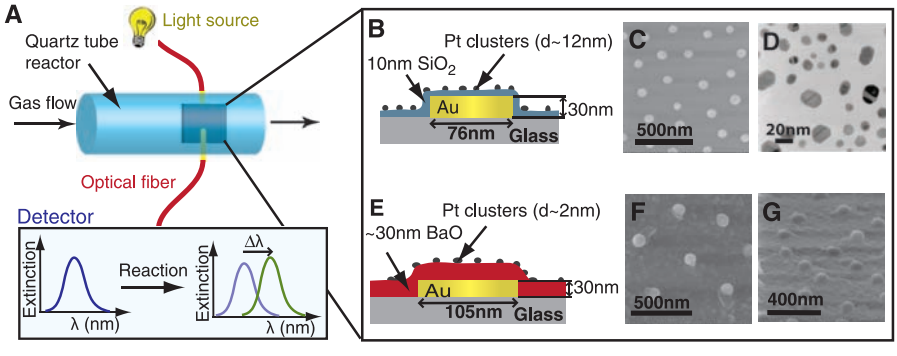

Fig. 1. Experimental setup and sensing structures (*7*). (**A**) Flow reactor arrangement and (bottom) optical readout. (**B**) Catalyst and sensing structure used to monitor changes in adsorbate coverage. (**C**) Scanning electron microscopy image of the sensing structure in (B). (**D**) TEM image of Pt catalyst clusters identical to those on the sensing structure in (B). (**E**) Sensing structure used to monitor the NO_2 storage/release from BaO. (**F** and **G**) Top-view (F) and 70° tilt (G) SEM images of the sensing structure in (E).

We next explored the practically important and most-studied catalytic model reaction CO + O_2 (*17*) in the same way as for H_2 + O_2, using the same Pt catalyst sample. A representative example is shown in Fig. 2B (8% reactants, 506 K, and 16.7 ml/min). As in the H_2 + O_2 reaction, an almost discontinuous step in $\Delta\lambda_{max}$ occurs of nearly the same amplitude but for a mixing ratio of α^{CO} = [CO]/([CO] + [O_2]) around 0.07. This is the kinetic phase transition in the CO + O_2 reaction from an oxygen- to a CO-covered surface, which is known to occur at very low relative CO concentration (*18*), much lower than for the H_2 + O_2 reaction, which explains the small $\alpha^{CO}{}_{cr}$ value. The kinetic phase transition and the associated coverage change can be sensitively detected with LSPR sensing.

A difference from the H_2 + O_2 reaction is that the temperature versus α profile is asymmetric around $\alpha^{CO}{}_{cr}$. This asymmetry arises from the strong blocking (poisoning) effect of CO for oxygen adsorption, preventing O_2 from dissociating and reacting when the surface is CO-saturated. Thus, the temperature profile is flat at $\alpha^{CO} > \alpha^{CO}{}_{cr}$, and there is no temperature-induced slope of the wing of $\Delta\lambda_{max}$, such as for H_2 + O_2 in Fig. 2A, because there is no reaction and no chemical energy dissipated, and the coverage is fixed at 1 ML CO. Similar behavior (an asymmetric *T* versus α peak) was seen also for the H_2 + O_2 reaction, but at lower temperatures [supporting online material (SOM) text]. The latter is caused by hydrogen poisoning (*13*) of the reaction at low temperature, similar to CO poisoning for the CO reaction. This occurs at lower temperature for the hydrogen reaction because the chemisorption energy is much smaller for hydrogen as compared with CO.

As seen in Fig. 2B, there is an irreversibility in closing the cycle going from oxygen-rich to CO-rich and back to oxygen-rich conditions. The origin of this is probably some irreversibility in the oxidation-reduction cycle. This minor effect does not change the main analysis of the $\Delta\lambda_{max}$ step at the kinetic phase transition point. Carbonyls or other similar poisoning effects were ruled out because they would have monotonically reduced the activity of the samples, which was not the case.

We now turn to a more complex but practically important reaction in automotive emission cleaning for diesel and so-called "lean burn" engines (engines operated at oxygen excess) in which the conventional three-way catalyst cannot reduce NO_x efficiently. The latter has led to the development of so-called NO_x storage/reduction catalysts, in which NO_x is temporarily (~1 min) accumulated in the catalyst, whereas the engine operates at O_2 excess [typically 30 to 600 parts per million (ppm) levels of NO + NO_2], and then the stored NO_x is reduced to N_2 by switching the air/fuel mixture to excess fuel, HC (or H_2), for a few seconds. A key to this solution is the NO_x storage material, usually barium oxide (BaO), which upon NO_x storage is converted to $Ba(NO_3)_2$ or related compounds (*6*). Pt (and in practice usually also Rh) is needed for the reduction step and also for oxidation of NO (when present) to NO_2 during the storage phase.

To test whether LSPR detection can monitor these reactions, we used a similar catalyst and sensing structure as above but with the passive SiO_2 layer replaced by an evaporated, ~30-nm-thick NO_x-active BaO layer (Fig. 1, E to G) deposited over the Au LSPR-sensing particles (140 nm diameter, 30 nm high, and $\lambda_{max} \approx 660$ nm). A similar nanogranular Pt film as above was then deposited on the BaO film (*7*). To mimic the NO_x storage period, the sample was exposed for 30 min to a gas mixture of 30 to 1000 ppm NO_2 + 6% O_2. It was subsequently exposed to 2% H_2 to mimic the reduction period, in which the catalyst is restored to be able to store NO_X again.

The results of both the storage period (*t* = 8 to 38 min in Fig. 3) and the reduction step are shown in Fig. 3A. For all curves, there is an initial rapid upward shift of $\Delta\lambda_{max}$ within 20 s after exposure to NO_2 and O_2 and then a slowly continuing increase, which is greater for higher NO_2 concentrations. We interpret this as LSPR detection of the BaO + NO_2 storage reaction, converting a thin surface layer of BaO to $Ba(NO_3)_2$, which changes the effective refractive index that is sensed by the LSPR sensor (see below). The larger signals for larger NO_2 concentrations (quantified in Fig. 3B) are caused by a combination of reversible and irreversible NO_x storage, both increasing with increasing NO_x concentration. Exposing the sample to H_2 (at 38 min in Fig. 3A) results as expected in a shift of $\Delta\lambda_{max}$ back to the original value before the NO_2 exposure because of the hydrogen reduction of stored NO_x to N_2 and concerted $Ba(NO_3)_2$ → BaO conversion (creating partly reduced BaO). The immediate shift also at 0 ppm NO_2 is due to the oxidation of the partially reduced BaO in the presence of O_2 after the hydrogen treatment.

Regarding the sensing mechanisms, in the sensing of the kinetic phase transitions for the CO and H_2 reactions (Fig. 2) the major change is a conversion of the adsorbate layer on the Pt nanoparticles from (or to) an oxygen-saturated to (or from) a CO- or (partially) hydrogen-covered surface. Oxygen adsorption/removal on Pt involves charge rearrangement in the surface layer manifested, for example, in a change of work function (*19*, *20*). In the standard treatment of LSPR sensing (*4*), this charge rearrangement can be associated with a change in the dielectric properties of the surface layer. Based on the collected data for the indirect sensing examples, including calibration data (SOM text) (*7*), we conclude that the oxygen-coverage change is the main contributor to the measured shift in $\Delta\lambda_{max}$, whereas the CO and H coverages have less influence (although they create a measurable signal, at least for CO). From the observed $\Delta\lambda_{max}$ shifts of ~1 nm (Fig. 2) and the spectral resolution in the experimental setup, we estimate a lower sensitivity limit for the current measurements with the same type of sample to be 0.02 monolayer of oxygen. For a more detailed discussion on sensitivity and how it compares with other studies (*21*–*25*), see the SOM text. We estimate that this sensitivity can be improved down to around 0.001 monolayer by use of improved optical measurements (*26*) and even further by optimizing the sensing structure (SOM text). This estimate is for a Pt coverage of only ~20% on the sample surface. This sensitivity is high enough to detect similar coverage changes with a real supported catalyst, which in addition can be a three-dimensional (3D) porous structure with more catalytic material within the LSPR sensing range. The sensing volume is estimated to extend to at least 20 nm away from the Au sensing particles. With a nanoporous support with supported particles in the <5-to-10-nm range, several monolayers of nanoparticles would thus be sensed. Such a structure would also represent a very typical catalyst structure. Work is in progress to make measurements with such structures.

In the NO_x sensing, the Pt/BaO/Au–LSPR structure senses changes in the dielectric constant near the Au particles, which is caused by incorporation of NO_x in the BaO layer. The corresponding LSPR signal is approximately an order of magnitude greater than for the CO and H_2 reactions; this is a very sensitive (and fast) method for NO_x sensing. We attribute the larger signal to a combination of three effects: (i) the involved surface area is greater, close to 80 to 90% as compared with 20%, because only a minor part of the BaO is covered by Pt; (ii) there is most likely a 3D rather than 2D NO_x layer involved in the storage (*27*); and (iii) the volume

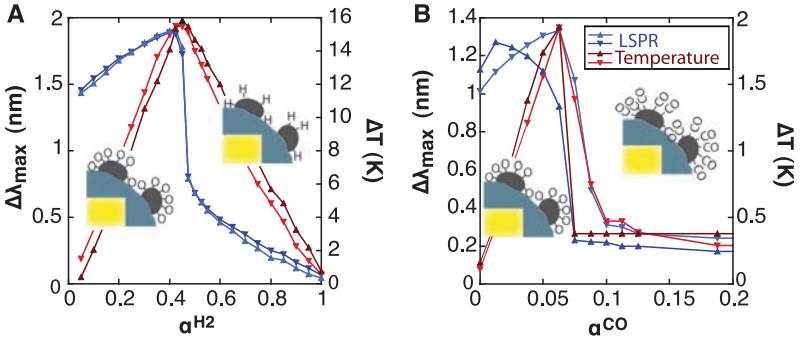

Fig. 2. Plasmon peak shift (blue) and temperature variation (red) during α^{H2} and α^{CO} sweeps. The indirect sensing structure in Fig. 1, B to D, was used. Triangles pointing up and down represent α sweeps up and down, respectively. (**A**) α^{H2} sweeps at 509 K, 4% H_2 + O_2 reactant, and 16.7 ml/s. The pictures to the left and right of the step in $\Delta\lambda_{max}$ illustrate the change in surface coverage upon passing the kinetic phase transition. (**B**) α^{CO} sweeps at 506 K, 8% CO + O_2 reactant, and 16.7 ml/s.

expansion upon NO_x storage is very large, causing a large change in overall dielectric response.

Although demonstrated here for only two materials, one metal and one nonmetal (Pt and BaO), there is in principle no limitation with respect to the catalytic materials for which the indirect sensing can be applied because the basic principle is that a change in surface coverage—in the composition of the chemisorption or thin surface layer—causes a change in the polarizibility/dielectric properties of that layer, which is sensed by the LSPR. This statement is generic and applicable to all catalytic materials. What may vary is the absolute sensitivity to different combinations of materials and chemisorbed molecules, which in turn will influence the sensitivity and degree of applicability of the method. Also, the material in the separating layer imposes no restriction, except possibly from a technical point of view, because any dielectric of interest as a catalyst support such as alumina, titania, zirconia, iron oxides, or various carbides, will work similarly well as SiO_2. This lack of limitation regarding the support material derives from the ability of the LSPR-induced electromagnetic field to penetrate through the separating layer and sense changes in the coverage of the actual catalyst particles, which in turn induces a LSPR frequency shift that is measured. It is in practice therefore the ability to make thin separating layers of various materials, rather than their dielectric properties, that may impose some limitations.

We are not claiming that the method is applicable to every situation; few methods are. However, we claim to have demonstrated a method with high potential for many important situations in catalysis. Regarding limitations, they may occur for reactions with mixtures of several reactants that have substantial coverage simultaneously or very low total coverage. However, the opposite cases are abundant in catalysis. For example, many catalytic reactions are, even under practical conditions, dominated by the coverage of one species, and the coverage frequently changes from dominance of one species to dominance of a second species at the rate maximum. For more complex situations, multiplexing approaches (as discussed below and in the SOM text) may be used.

The very high sensitivity of the LSPR sensing as demonstrated here is mainly a virtue but potentially also a cause of interpretation problems in some cases. For example, catalyst restructuring and changes of the support may interfere with the detection of the actual coverage changes of interest (in other situations, it might be these side effects that are of interest to measure). However, there are several ways of dealing with these and similar effects, if at hand. (i) Irreversible restructuring can be detected by returning to an identical reaction situation (such as temperature or coverage) and noting the corresponding LSPR shifts. (ii) Such effects can, as was done in the present measurements, be eliminated by using the common "running in" approach in catalysis, in which the catalyst is cycled through the reaction conditions several times before the actual measurements are done in order to stabilize the catalyst structurally and chemically. (iii) Temperature effects can be calibrated away (see above). (iv) Support effects can be calibrated away (see above and SOM text). (v) However, for the future, a more elegant approach would be to build in such eliminations by means of multiplexing—by using different areas on a single sample, with each area optimized to detect one change or correction of interest. The parameters at hand for such multiplexing are, for example, the size and shape of the sensing Au (or other material) LSPR particles and the thickness of the separating layer while keeping the actual catalyst particles the same everywhere. LSPR is ideal for such an approach because very small areas are required for each measurement area (such as 10 by 10 μm) and because parallel detection is possible through spectroscopic imaging. For example, one area of the multiplexing structure could then be optimized for coverage monitoring, another for temperature measurement, and yet another to monitor support interactions. Some such functions may even be achieved by using elongated sensing particles and two light polarizations, as demonstrated in (*28*), because the short and long particle directions have different spectral sensing regions and probably also different relative sensitivity factors for, for example, adsorbates and temperature.

The sensing structures we used have not been optimized with respect to shape, size, and material of the LSPR-sensing particles or of the separating layer. For example, it is possible to improve the sensitivity by optimizing the thickness of the SiO_2 (or other oxide) layer (*29*) between the sensing particles and the actual catalyst. The same type of structures as described here can also be combined with simultaneous, LSPR-enhanced Fourier transform infrared (*30*) or Raman spectroscopy (*31*), which would provide simultaneous spectroscopic information about specific adsorbates or adsorbate-substrate bonds.

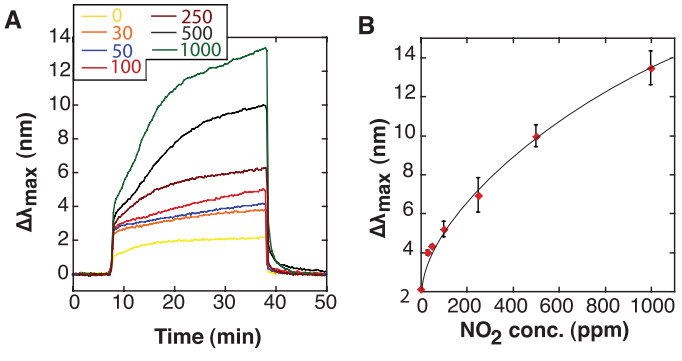

Fig. 3. NO_x storage and release (as N_2) from BaO measured with the catalyst structure in Fig. 1, E to G. (**A**) Plasmon peak shift during 30 min NO_2 storage (at t = 8 to 38 min), at seven different concentrations (0, 30, 50, 100, 250, 500, and 1000 ppm), and subsequent release by exposure to 2% H_2 (at t = 38 min). (**B**) Total plasmon peak shift after 30 min of NO_2 exposure as a function of NO_2 concentration [same concentrations as in (A)].

References and Notes

1. G. Ertl, *Angew. Chem. Int. Ed.* **47**, 3524 (2008).
2. G. A. Somorjai, J. Y. Park, *Catal. Lett.* **115**, 87 (2007).
3. D. W. Goodman, *Chem. Rev.* **95**, 523 (1995).
4. J. N. Anker *et al.*, *Nat. Mater.* **7**, 442 (2008).
5. S. Völkening, K. Bedurftig, K. Jacobi, J. Wintterlin, G. Ertl, *Phys. Rev. Lett.* **83**, 2672 (1999).
6. N. Takahashi *et al.*, *Catal. Today* **27**, 63 (1996).
7. Materials and methods are available as supporting material on *Science* Online.
8. U. Kreibig, M. Vollmer, *Optical Properties of Metal Clusters: Springer Series in Materials Science* (Springer Verlag, Berlin, 1995), vol. 25.
9. H. Fredriksson *et al.*, *Adv. Mater.* **19**, 4297 (2007).
10. C. Langhammer, E. Larsson, I. Zoric, B. Kasemo, Swedish Patent application P18030SE00 (2009).
11. C. Novo, A. M. Funston, P. Mulvaney, *Nat. Nanotechnol.* **3**, 598 (2008).
12. M. Wallin, H. Grönbeck, A. Lloyd Spetz, M. Eriksson, M. Skoglundh, *J. Phys. Chem. B* **109**, 9581 (2005).
13. V. P. Zhdanov, B. Kasemo, *Surf. Sci. Rep.* **20**, 111 (1994).
14. G. Weick, G.-L. Ingold, R. A. Jalabert, D. Weinmann, *Phys. Rev. B* **74**, 165421 (2006).
15. C. Langhammer, Z. Yuan, I. Zoric, B. Kasemo, *Nano Lett.* **6**, 833 (2006).
16. K. Wong, S. Johansson, B. Kasemo, *Faraday Discuss.* **105**, 237 (1996).
17. G. Ertl, *Surf. Sci.* **299–300**, 742 (1994).
18. M. Bär, C. Zulicke, M. Eiswirth, G. Ertl, *J. Chem. Phys.* **96**, 8595 (1992).
19. D. H. Parker, M. E. Bartram, B. E. Koel, *Surf. Sci.* **217**, 489 (1989).
20. G. A. Somorjai, M. A. Van Hove, *Prog. Surf. Sci.* **30**, 201 (1989).
21. G. H. Chan, J. Zhao, E. M. Hicks, G. C. Schatz, R. P. Van Duyne, *Nano Lett.* **7**, 1947 (2007).
22. C. Langhammer, M. Schwind, B. Kasemo, I. Zori, *Nano Lett.* **8**, 1461 (2008).
23. E. M. Larsson, J. Alegret, M. Käll, D. S. Sutherland, *Nano Lett.* **7**, 1256 (2007).
24. T. Rindzevicius *et al.*, *Nano Lett.* **5**, 2335 (2005).
25. L. J. Sherry, R. C. Jin, C. A. Mirkin, G. C. Schatz, R. P. Van Duyne, *Nano Lett.* **6**, 2060 (2006).
26. A. B. Dahlin, J. O. Tegenfeldt, F. Hook, *Anal. Chem.* **78**, 4416 (2006).
27. J. Szanyi, J. H. Kwak, D. H. Kim, S. D. Burton, C. H. F. Peden, *J. Phys. Chem. B* **109**, 27 (2005).
28. C. Hagglund, M. Zach, G. Petersson, B. Kasemo, *Appl. Phys. Lett.* **92**, 053110 (2008).
29. T. Rindzevicius, Y. Alaverdyan, M. Käll, W. A. Murray, W. L. Barnes, *J. Phys. Chem. C* **111**, 11806 (2007).
30. D. Enders, T. Nagao, T. Nakayama, M. Aono, *Langmuir* **23**, 6119 (2007).
31. S. Nie, S. R. Emory, *Science* **275**, 1102 (1997).

32. The Swedish foundation for strategic research (program PhotoNano), the Chalmers Foundation, and the Swedish energy agency (project N2E2) are acknowledged for their financial support. We are grateful to S. Gustafsson and E. Olsson at our department for the TEM picture in Fig. 1D.

Supporting Online Material

www.sciencemag.org/cgi/content/full/1176593/DC1
Materials and Methods
SOM Text
Figs. S1 to S6
References

20 May 2009; accepted 8 September 2009
Published online 22 October 2009;
10.1126/science.1176593
Include this information when citing this paper.